

Article

Coal Anisotropic Sorption and Permeability: An Experimental Study

Yulong Chen ¹, Xuelong Li ^{2,*} and Bo Li ^{3,*}

¹ State Key Laboratory of Hydrosience and Engineering, Tsinghua University, Beijing 100084, China; chen_yl@tsinghua.edu.cn

² State Key Laboratory of Coal Mine Disaster Dynamics and Control, Chongqing University, Chongqing 400030, China

³ Key Laboratory of Karst Environment and Geohazard, Ministry of Land and Resources, Guizhou University, Guiyang 550000, China

* Correspondence: lilxcumt@126.com (X.L.); libo1512@163.com (B.L.)

Received: 27 June 2018; Accepted: 23 July 2018; Published: 30 July 2018



Abstract: Knowledge of the bedding plane properties of coal seams is essential for the coalbed gas production because of their great influence on the inner flow characteristics and sorption features of gas and water. In this study, an experimental study on the anisotropic gas adsorption–desorption and permeability of coal is presented. The results show that during the adsorption–desorption process, an increase in the bedding plane angle of the specimen expands the length and area of the contact surface, thereby increasing the speed and quantity of adsorption and desorption. With an increase in the bedding angle, the number of pores and cracks was found to increase together with the volumetric strain. The evolution of permeability of coal heavily depended on stress–strain stages. The permeability decreased with the increase of stress at the initial compaction and elastic deformation stages, while it increased with the increase of stress at the stages of strain-hardening, softening and residual strength. Initial permeability increased with increasing bedding angle.

Keywords: anisotropy; bedding plane orientation; coal; gas; adsorption–desorption

1. Introduction

Coalbed gas extraction has been considered as an attractive solution to control coal-mine disasters and provide new energy, and it has found great success in many countries (e.g., Australia, Canada). Coalbed gas extraction is a complicated process that is influenced by many factors, such as the mechanical properties of the formation (e.g., modulus, strength), sorptive capability, and transport properties (e.g., diffusivity, permeability) [1]. A better understanding of mechanical behavior and transport properties of coal is necessary to optimize field development. Among the transport properties, sorption and permeability are the most important parameters to influence gas production in coalbed gas formations [2–4].

A significant number of studies [5–10] have been conducted to investigate coal sorption and permeability under different conditions. It is found that coal sorption and permeability is impacted by many factors, such as fracture geometry [11–13], stress [14–16], water content [17,18], and temperature [19,20]. These experiments have focused on the isotropic characteristics of intact or powdered coals.

As a sedimentary rock with cleats, coal exhibits a notable anisotropic geometry and anisotropic mechanical properties [21,22]. The gas adsorption–desorption and permeability properties of coal are also found to be anisotropic [23], although many studies consider coal sorption and permeability as isotropic to simplify the analysis [13]. The anisotropic gas adsorption–desorption and permeability of coal remain unclear. To gain a better understanding of these two issues, an experimental study was

carried out, and detailed results on the anisotropic gas adsorption–desorption and permeability of coal are presented in this study.

2. Experimental Method

In this study, a coal block was taken from the #7 coal seam in the Dabaoding coal mine in Sichuan Province, China. High-quality thermal coal was present with medium and ash, and had good thermal stability and high calorific value. The main characteristic parameters of coal are shown in Table 1.

Table 1. Status table of coal.

Index	Value
Moisture content (%)	0.71
Ash content (%)	10.11
Volatile matter content (%)	12.01
C (%)	90.91
H (%)	3.94
O (%)	2.54
N (%)	1.44

A series of cylindrical samples with a diameter of 50 mm and a length of approximately 100 mm were machined from this coal block. The coal samples were categorized based on the included angle β between the radial direction of the drill and the direction of the bedding surface, namely $\beta = 0^\circ$, 30° , 60° , and 90° , as shown in Figure 1.

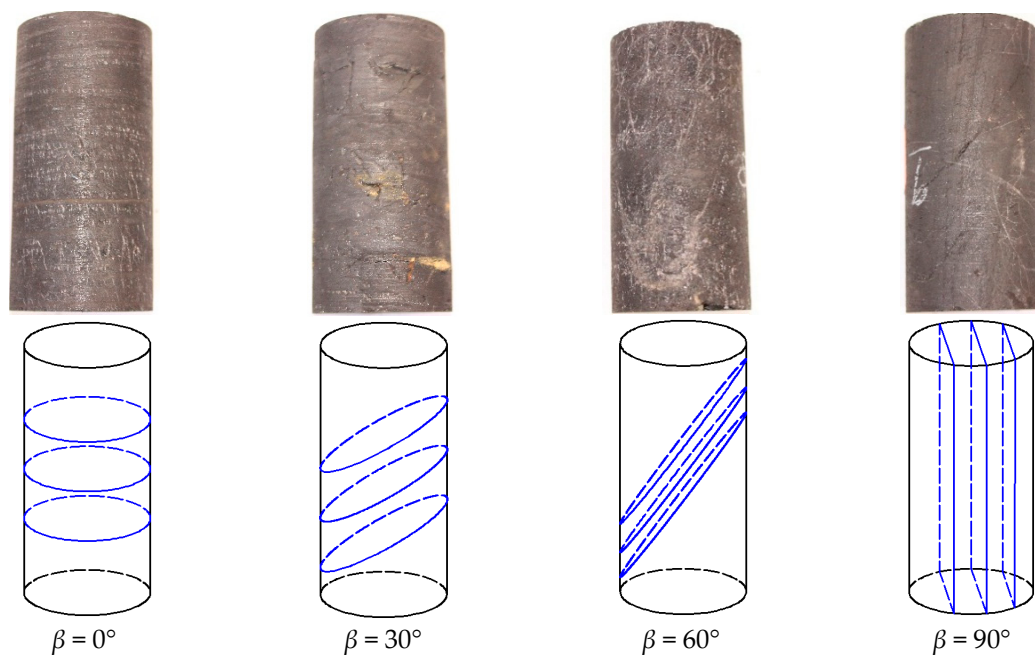


Figure 1. Coal samples and corresponding bedding angles.

Gas adsorption–desorption and permeability tests were performed on the prepared coal samples using a triaxial cell. Figure 2 shows the apparatus, where Figure 2a shows the main components: confining pressure and gas pressure control system, seepage pipe and holder system and automatic data recording system. Figure 2b is a photo of this apparatus. This cell is capable of accepting membrane-sheathed cylindrical samples (50 mm diameter). Axial and hydrostatic stresses up to 56 MPa were independently applied using two ISCO-260D pumps (Teledyne ISCO, Lincoln, NE, USA) with control up to 61 kPa. The gas pressure in the upstream was controlled by an ISCO-500D pump.

The flow rate was measured using a mass flowmeter with an accuracy of 4 mL/min. The flowmeter was connected with the outlet end of the fluid pipelines and the atmosphere. Temperature was controlled, and its variation was within ± 0.1 °C during testing.

The cylindrical sample was inserted into a polyvinyl chloride (PVC) rubber jacket and then sandwiched in the holder by two cylindrical stainless-steel loading platens. The two platens with through-going flow connections and flow distributors were respectively connected with both ends of the triaxial cell.

Coal is sensitive to water [24,25]; it not only reduces the effective porosity but also induces swelling of the coal matrix. To minimize the effect of water on coal, the samples were dried in a vacuum oven at 70 °C for two days before performing the gas adsorption–desorption and permeability tests. It is preferable to dry samples at lower temperatures for a longer time rather than at a high temperature for a shorter time because cracks or mineral alterations can occur at high temperatures [26]. To reduce the discreteness of the test data, three samples of coal, which have no macroscopic cracks, are of similar quality and have uniform features during CT scanning, were selected for the experiments. The details of the tests are described in the following section.

- Gas adsorption–desorption experiment: The samples were placed in the triaxial cell and subjected to negative pressure for 24 h. Next a gas injection pressure of 3 MPa and confining pressure of 3 MPa were applied for gas adsorption for 24 h. Subsequently, gas was desorbed until the desorption balance was achieved when the pressure was reduced to 0.5 MPa.
- Stress–strain–permeability experiment: Samples were placed under a confining pressure of 3 MPa at a speed of 0.1 MPa/s. Gas was allowed to enter the samples under a pressure of 2 MPa, which was maintained for 30 min with stable gas flux. Then the confining pressure and gas pressure were maintained, and the gas flux was monitored while the axial stress was continuously applied by stress control at a speed of 0.05 MPa/s until coal specimen failure. After failure, the stress control shifted to displacement control at a speed of 0.1 mm/min until the residual strength of the samples remained stable.

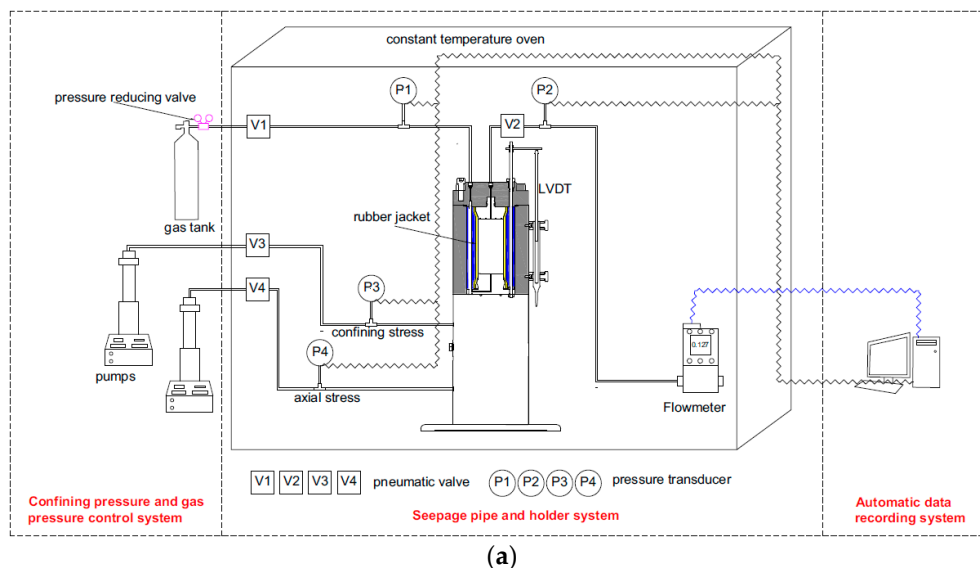


Figure 2. Cont.

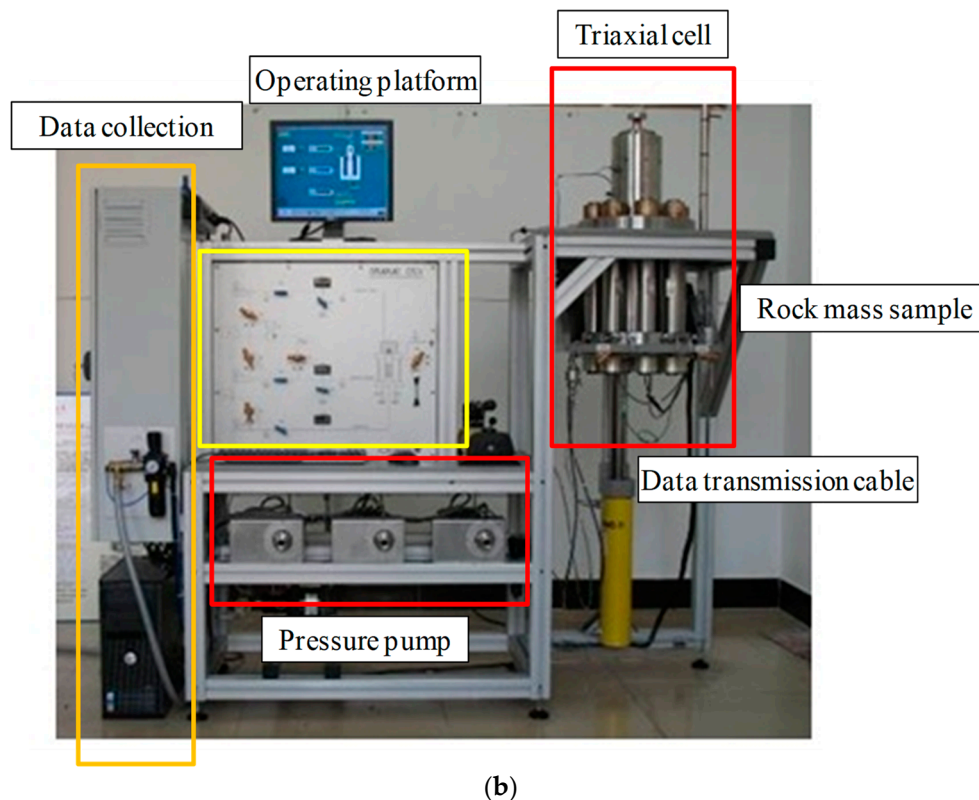


Figure 2. (a) Schematic diagram; (b) Experimental apparatus.

3. Results

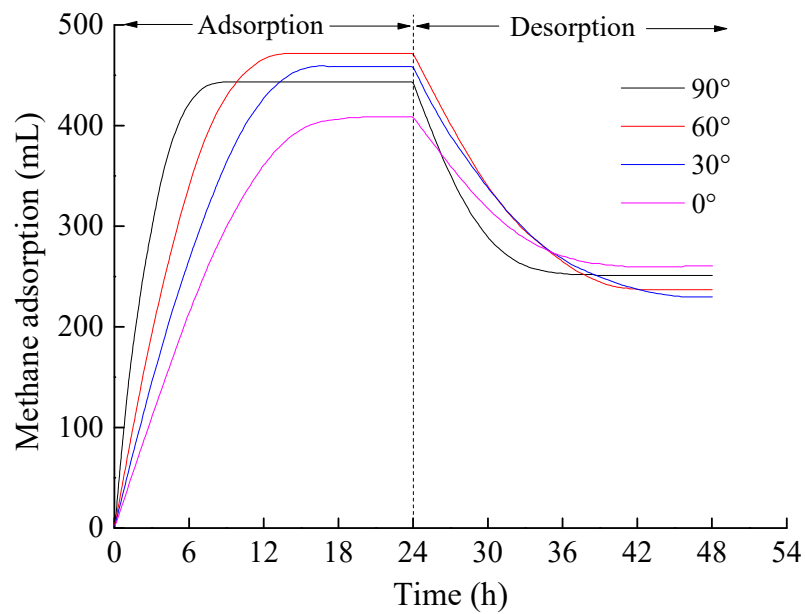
3.1. Adsorption–Desorption Experiment

The final adsorption capacity, desorption capacity, and deformation of the samples are presented in Table 2. The raw coal samples exhibited strong heterogeneity during the adsorption–desorption process test. Even for those samples with the same bedding angle, the adsorption–desorption characteristics might still be different. Some differences emerged in the results among samples with the same bedding angles, but the differences of adsorption and desorption capacity and deformation were within 10%. This pattern indicates that the specific surface area of the matrix and the Van der Waals force for the samples were similar. Under the same adsorption–desorption pressure, pores in the matrix had the same ability to adsorb gas for the different samples. Therefore, the volumetric strain appeared to be similar for samples with different angles because all samples adsorbed equal amounts of gas.

A comparison of the standard adsorption–desorption curves for samples with different bedding angles is shown in Figures 3 and 4. After the gas entered the samples at 3 MPa of pressure, the interior of each sample was in a state of negative pressure. Due to the pressure difference and concentration difference, gas began to seep in and diffuse quickly; once the gas had seeped into a sample, the gas pressure difference and concentration difference gradually decreased, thus reducing the adsorption speed until a saturation state was reached. Gas desorption is the inverse process of gas adsorption; however, because microstructures existed within the coal, microcracks and pores of the coal matrix could close and affect the seepage and diffusion channels. Ultimately, the desorption quantity was reduced to less than 50% of the adsorption quantity, and the time to reach the desorption balance was twice that required for adsorption.

Table 2. Final adsorption capacity, desorption capacity, and deformation of the samples in the adsorption–desorption experiment.

Bedding Angle	Adsorption Capacity (mL)	Desorption Quantity (mL)	Volumetric Strain after Adsorption ($\mu\epsilon$)	Volumetric Strain after Desorption ($\mu\epsilon$)
0°	400	217	−1427	−337
	440	196	−1839	−279
	470	286	−2101	−310
30°	391	252	−1866	−286
	455	182	−1927	−310
	470	202	−1900	−347
60°	450	220	−1409	−382
	431	179	−1988	−315
	467	218	−1845	−336
90°	500	210	−1280	−299
	408	184	−1543	−340
	425	211	−1994	−326

**Figure 3.** Gas adsorption–desorption over time.

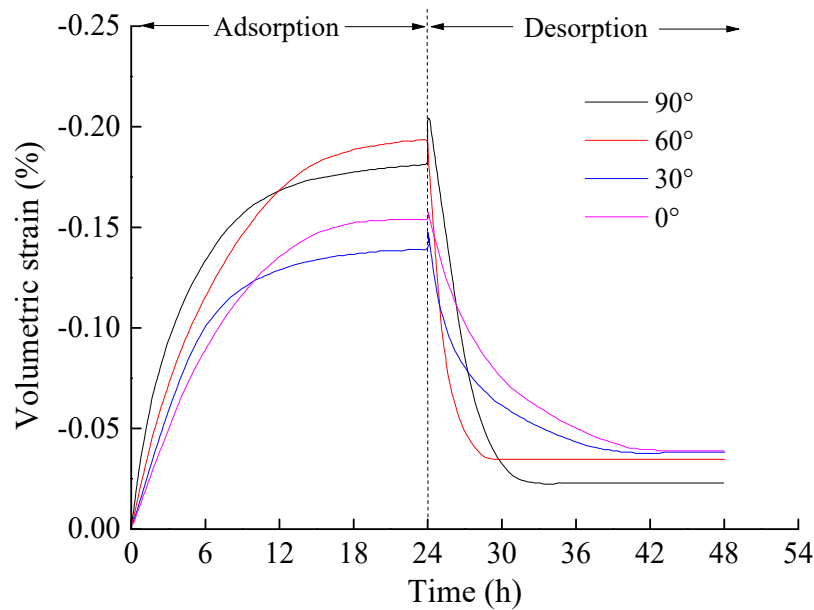


Figure 4. Volumetric strain during the gas adsorption–desorption process.


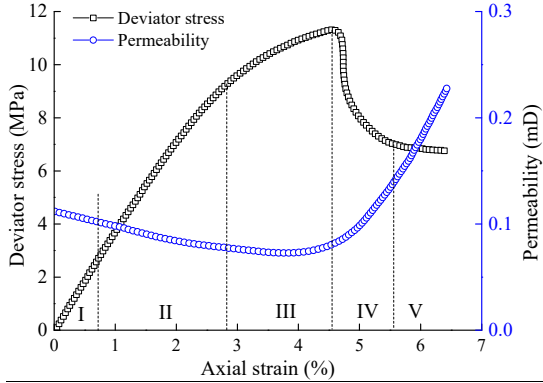

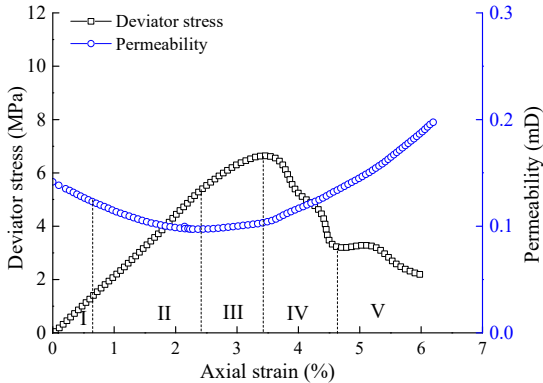

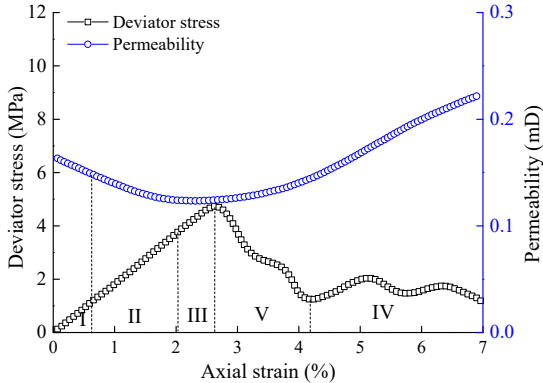

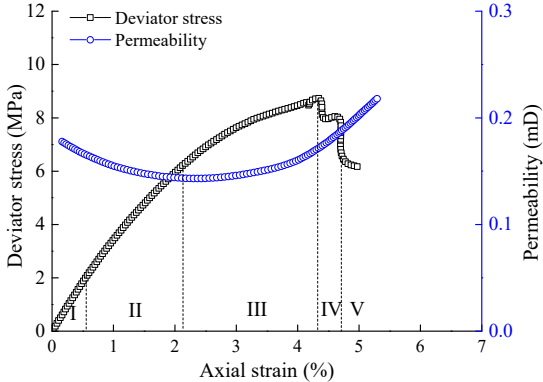
The adsorption–desorption process of samples at different bedding angles exhibited certain differences. As shown in Figure 3, for the same adsorption time, gas adsorption was fastest for the sample with a 90° angle. The time to reach adsorption stability for this sample was half that required for the sample with a 0° angle; the adsorption time was shorter for the sample with a 60° angle than for that with a 30° angle. The gas adsorption speed was the lowest at an angle of 0° . The gas adsorption quantities of the samples when $\beta = 0^\circ, 30^\circ, 60^\circ$, and 90° were 440 mL, 470 mL, 450 mL, and 408 mL, respectively. Little difference therefore existed in the adsorption amounts, but the bedding angle was influential. Regardless of the adsorption or desorption process, the larger the bedding angle, the faster the adsorption or desorption.

Gas adsorption and desorption processes at a macroscopic level represent interactions occurring in the coal microstructure. The reason for such significant differences in the length and area of the bedding surface and the crack distribution could be the different bedding angles. The facet length and contact surface area of the bedding plane increased as the angle increased. Although the samples exhibited strong anisotropy with regard to volumetric strain during the adsorption–desorption process, volumetric strain increased in line with the bedding angle. These pores and cracks provided a seepage channel and a contact surface for adsorption in the inner matrix of the sample, which facilitated gas adsorption. The larger the bedding angle of the samples, the larger the pores and cracks, which explains why the gas adsorption–desorption speed increased as the bedding angle increased while the adsorption amount and volumetric strain remained the same.

3.2. Stress–Strain–Permeability Experiment

Many geotechnical engineering practices and experimental results have demonstrated that coal permeability is closely related to its stability and failure mode. During the process of becoming unstable (i.e., as cracks develop and failure occurs), the degree of extension of the original joint crack and its ongoing development determine the seepage features of gas in coalbed. The existence of bedding joints has been shown to greatly influence the mechanical properties of coal samples. Among multiple experiments, this study selected a representative sample, shown in Table 3.

Table 3. Photos of post-compression specimens and stress–strain–permeability curves.

Bedding Angle	Failure Mode	Failure Pattern	Stress–Strain–Permeability
0°	Splitting failure		
30°	Compound shear and splitting failure		
60°	Shear failure		
90°	Splitting failure		

3.2.1. Axial Stress–Axial Strain–Permeability Curve of Coal

The compression experiment of samples with different angles demonstrated the stress–strain relationship and corresponding permeability–strain relationship, the forms of which were fundamentally consistent. After considering the relationship of these two curves, $\beta = 0^\circ$ was used as an example; the stress–strain curve and permeability–strain can be divided into five stages and are denoted as I–V in Table 3.

(1) Initial compaction stage: The stress–strain curve moved upward slightly, and the primary pores and cracks in the coal sample gradually closed under pressure; this change decreased the gas seepage channels and resulted in reduced permeability.

(2) Elastic deformation stage: The stress–strain curve was nearly straight. Due to higher loading, the primary pores and cracks inside the coal sample continued to shrink. Shear and tensile stresses created new microcracks on the sample. This stage is the stable extension stage of cracks; as the strain increased, the effects on new cracks increased and permeability decreased as evidenced by the permeability–strain curve.

(3) Strain-hardening stage: In this stage, the stress–strain curve exhibited significant nonlinearity. As the normal loading continued to increase, shear and tension cracks developed rapidly, leading to irreversible deformation. By this time, the permeability curve had reached its minimum and had begun to increase slowly. During this stage, more microcracks began to extend and connect, and permeability increased gradually.

(4) Strain-softening stage: After the bearing capacity of the coal sample reached peak strength, the inner structure was damaged, but the sample retained its overall shape. In this stage, stress declined rapidly. Tension and shear failure developed quickly, macroscopic fractures appeared on the surface, the sample became unstable, and failure occurred, as reflected in the permeability–strain relationship. The gas permeability increased substantially due to the creation of new cracks that provided seepage channels for the gas.

(5) Residual strength stage: The deformation of the sample consisted of slippage along the mass of macroscopic fractures; stress decreased and stabilized as strain increased. This pattern indicates that the damage and cracks due to compression increased, additional gas channels were created, and gas permeability continued to rise.

3.2.2. Mechanical Properties and Gas Permeability of Coal

Compression strength of coal is closely related to the bedding angle. Under conditions of loading and gas seepage, an increase in the bedding plane angle resulted in an initial decrease in the compressive strength of the sample followed by an increase. Compressive strength was largest at 11.5 MPa when $\beta = 0^\circ$. At $\beta = 30^\circ$ and $\beta = 60^\circ$, the compressive strength decreased to 5.5 MPa and 2.5 MPa, respectively. At $\beta = 90^\circ$, the compressive strength was 8.8 MPa, larger than the value for $\beta = 60^\circ$. This finding demonstrates that the mechanical property was anisotropic with regard to the bedding angle. The axial strain at peak strength, referred to as limit strain, was proportional to the peak strength; that is, the higher the peak strength, the higher the limit strain. The limit strain values of the four bedding angles were 4.6%, 3.4%, 2.5%, and 4.3%, respectively. The division between the brittleness and ductility of each sample was based on axial strain at peak strength; when the limit strain was lower than 1%, brittle failure occurred. Brittle ductile failure tended to occur in the range of 1–5%; all samples in this study exhibited brittle ductile failure.

As shown in Figures 5 and 6, the initial permeability varied widely among samples with different angles. Generally, initial permeability increased with an increase in the angle. The initial permeability values of the samples at angles of 30° , 60° , and 90° were respectively 1.27-, 1.46-, and 1.59-times that of the sample at an angle of 0° . As the axial load increased, axial strain and elastic energy increased as well. When the axial strain of the samples at angles of 0° , 30° , 60° , and 90° reached 0.9, 0.84, 0.7, and 0.5 of limit strain, respectively, gas permeability decreased to the respective minimum values of 0.0730 mD, 0.0973 mD, 0.124 mD, and 0.143 mD, representing 65%, 69%, 76%, and 80% of the initial permeability.

These results indicate that the original damage of the bedding plane of the coal sample affected the mechanical properties as well as permeability of the sample. The original damage to the coal sample involved the number of pores and cracks in the seam. If gas-containing coal samples possessed the same porosity, the degree to which fractures developed influenced the mechanical properties and seepage properties of the coal mass. As the gas permeability increased in line with the bedding angle, the number of seepage channels increased as well.

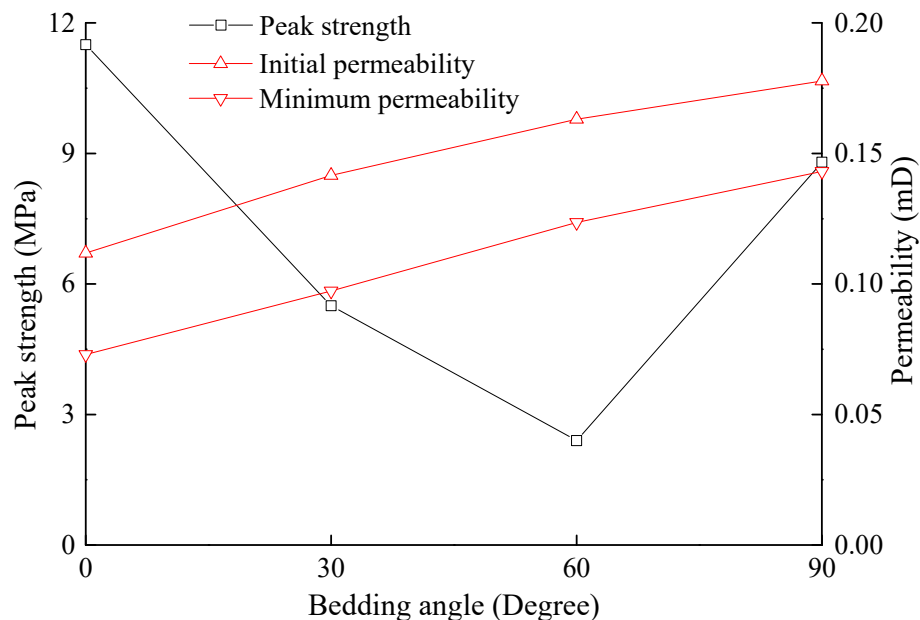


Figure 5. Peak strength and permeability at different bedding angles.

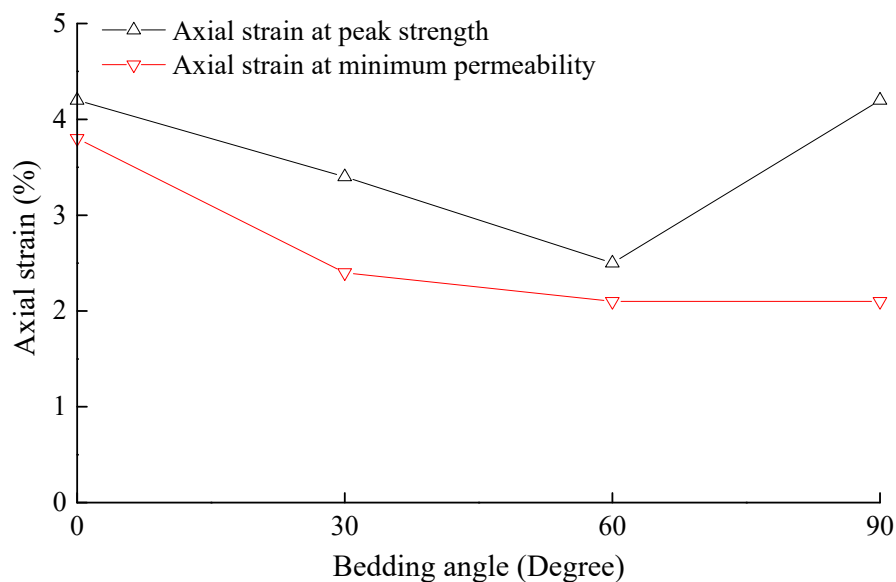


Figure 6. Axial strains at peak strength and minimum permeability at different bedding angles.

With an increase in axial strain, the pores in the matrix of the coal mass were compressed and gas seepage channels were affected, causing permeability to decline with an increase in stress. As a result, shear stress and tensile stress were apparently concentrated near the cracks in the interior of the sample, and the stress eventually extended to the surrounding area. The compression of pores in the matrix and crack extension occurred simultaneously. Once axial stress increased to a

certain value, the influence of the gas seepage channel extension became greater than that of the compression of cracks on permeability. After gas permeability reached its minimum, it increased as stress increased. However, for samples with different angles, large differences appeared in shear stress and tensile stress during compression; this finding resulted in clear differences between the stress–strain curves and permeability evolution curves. The cracks represented the main seepage channel of gas distribution; therefore, the bedding contact surface was easily damaged. As more cracks developed and extended, the effective area of the bedding contact surface increased. As the angle of the coal sample increased and gas permeability decreased to the minimum, the strain capacity was reduced; however, the compressive capacity of the coal sample at a 90° angle was apparently larger than that of the sample at the 60° angle.

3.2.3. Failure Mode of Coal

The coal samples experienced the highest loading values under peak stress, and cracks developed continuously during the loading process; the critical point of failure was reached at peak stress. After that, localized microcracks coalesced and propagated to form a fracture. The fracture occurred along the main crack in the coal sample, after which point the stress declined sharply. Due to local through-going cracks and stress release following from pore compression in the matrix, effective stress was reduced and gas seepage channels were extended at the same time. Therefore, gas permeability demonstrated a dramatic increase.

The bedding angle affected the macroscopic failure of coal samples as well as crack distributions, resulting in large differences in the failure mode and permeability of different samples. The following responses were observed. (1) When $\beta = 0^\circ$ and 90° , tensile splitting failure occurred, tensile stress affected the sample along the radial direction, and cracks appeared in the axial direction perpendicular and parallel to the bedding surface, respectively. The fracture was extensive, exhibiting numerous cracks. (2) When $\beta = 60^\circ$, shear slippage failure and a single main fracture occurred along the bedding surface. (3) When $\beta = 30^\circ$, the sample underwent compound shear and splitting failure. The crack began near the bedding plane and extended in the axial direction to the side end of the sample before ultimately splitting off the sample.

The bedding inclination caused some differences in the deformation and fracture properties, stimulating more complexity in the stress state along the bedding planes. The final failure mode of the sample reflected the influence of the bedding angle and was directly related to ultimate permeability. When $\beta = 0^\circ$, the elastic energy released intensively, and the fracture was severe; therefore, the change rate of permeability, and the final permeability when residual stress stabilized, was the largest of all samples. When $\beta = 90^\circ$, the sample was damaged by tension along the axial direction; dual splitting and cutting occurred in the sample, and the stress declined rapidly. Therefore, the final permeability was similar to the values of the sample with $\beta = 0^\circ$. When $\beta = 60^\circ$, due to the failure mode, the permeability did not exhibit a large jump, and the final permeability was smallest among all samples.

3.2.4. Relationship between Permeability, Radial Strain, and Volumetric Strain of Coal

Figures 7 and 8 illustrate the relationship between permeability, radial strain, and volumetric strain, respectively. For the same values of radial strain and volumetric strain, permeability increased with an increase in the angle.

Strong anisotropy was observed in the mechanical properties and seepage behaviors of samples with different bedding angles. The adsorption–desorption experiment excluded the effect of porosity on permeability under the loading condition. Moreover, the inclination of beddings induced shear stress near the plane; therefore, the bedding plane was the most probable location of crack initiation and propagation. Cracks occurred more easily along the surface of the bedding and then extended further before finally resulting in total failure of the entire specimen; as a result, the bedding plane

could form the most likely percolation channels to influence permeability. As such, the bedding plane should be considered when determining permeability.

In this section, the difference in permeability induced by the bedding angle was analyzed based on the plate fluid theory.

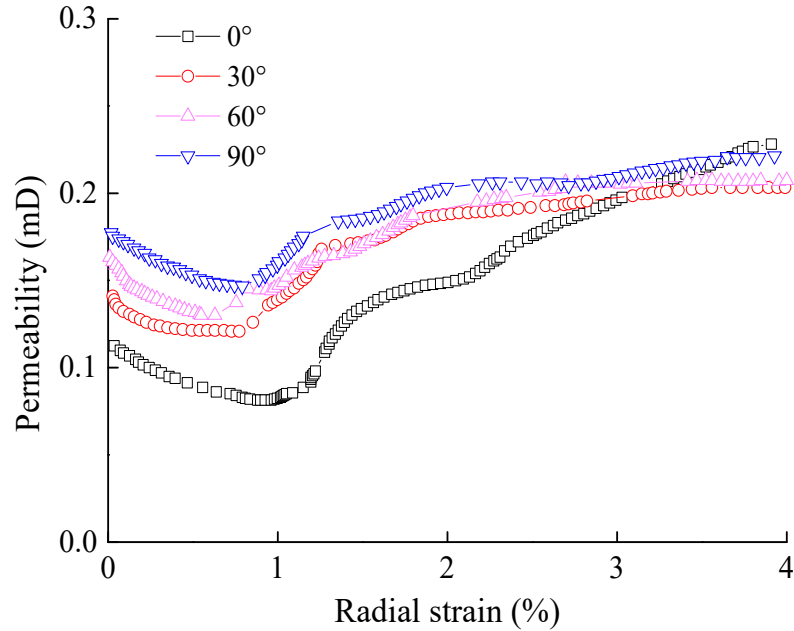


Figure 7. Relationship of permeability and radial strain.

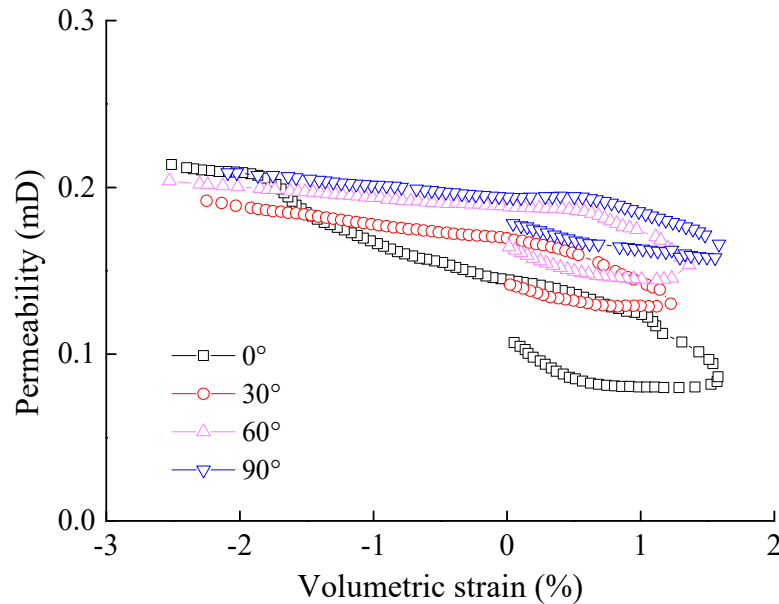


Figure 8. Relationship of permeability and volumetric strain.

The Hagen–Poiseuille flow function is written as follows:

$$Q = \frac{nd^3l(P_1^2 - P_2^2)}{12\mu hP_2}, \quad (1)$$

where n , d , l , and h denote the crack number (dimensionless), aperture (μm), length (m), and height (m), respectively. Q is the permeation rate (m^3/s), μ is the gas kinematic viscosity ($\text{Pa}\cdot\text{s}$), P_1 is the

gas pressure at the inlet of the specimen (Pa), and P_2 is the atmospheric pressure at the outlet of the specimen (Pa).

Darcy's law expresses the permeability k as

$$k = \frac{2\mu QLP_2}{A(P_1^2 - P_2^2)}. \quad (2)$$

Substituting Equation (1) into Equation (2) yields

$$k = \frac{nLLd^3}{6\mu Ah}. \quad (3)$$

When the sample deforms under stress, the radius R (m), height L (m), average aperture d_a (μm), length l_a (m), and height h_a (m) of the crack in the axial direction are respectively illustrated as=

$$\begin{cases} R = (1 - \varepsilon_r)R_0 \\ L = (1 - \varepsilon_a)L_0 \\ h_a = (1 - \varepsilon_a)h_{a0} \\ l_a = (1 - \varepsilon_r)l_{a0} \\ d_a = (1 - \varepsilon_r)d_{a0} \end{cases}, \quad (4)$$

where R_0 and L_0 refer to the initial diameter (m) and height (m) of the specimen, respectively; and h_{a0} , l_{a0} , and d_{a0} refer to the initial average height (m), length (m), and aperture (μm) of the crack, respectively.

Substituting Equation (4) into Equation (3) yields the relationship between permeability and radial strain,

$$k = \frac{L_0}{6\mu A_0} \frac{n_a l_{a0} d_{a0}^3}{h_{a0}} (1 - \varepsilon_r)^2, \quad (5)$$

where $\frac{L_0}{6\mu A_0}$ is the formal kinematic viscous coefficient α , which is a constant. $\frac{n_a l_{a0} d_{a0}^3}{h_{a0}}$ is defined as the initial crack coefficient β_a , which is linked to the axial initial crack aperture.

Equation (5) can be written as

$$k = \alpha \beta_a (1 - \varepsilon_r)^2. \quad (6)$$

Permeability is parabolically related to radial strain. The permeability–radial strain data of coal samples with different bedding angles were fitted using the parabolic equation as shown in Figure 9, indicating that the parabolic equation clearly described the permeability–radial strain data of coal with different bedding angles.

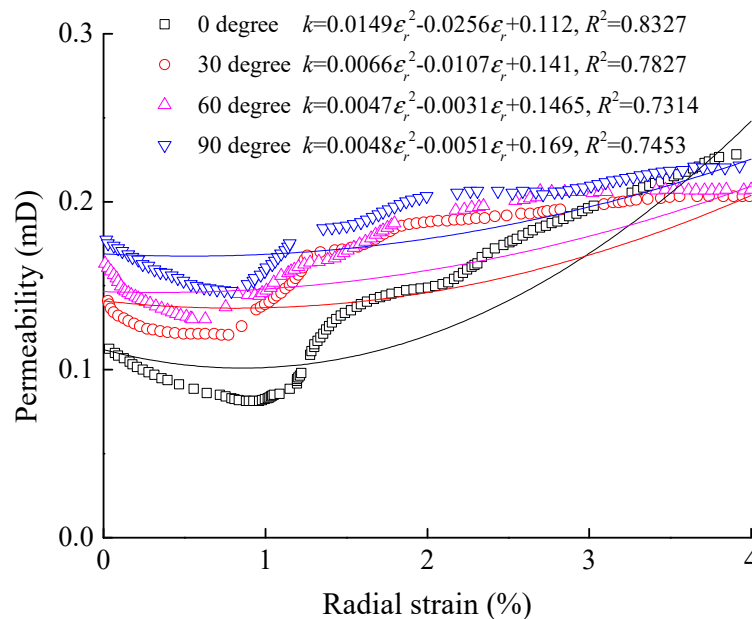


Figure 9. Fitting of permeability–radial strain data of coal samples with different bedding angles.

4. Conclusions

This study focused on the anisotropic adsorption–desorption and permeability of coal. A series of gas adsorption–desorption and permeability measurements were performed on specifically prepared coal samples. The following conclusions can be drawn from the experimental results:

(1) During the gas adsorption–desorption process, the length and area of the bedding contact surface of the sample increased with an increase in the bedding angle, resulting in faster adsorption/desorption.

(2) The larger the angle of the bedding plane in the sample, the larger the number of effective pores and cracks available for a seepage channel and a contact surface for adsorption in the inner matrix of the sample, which facilitated gas adsorption.

(3) The evolution of permeability varied across different stress–strain stages. Permeability declined with an increase in stress at the initial compaction and elastic deformation stages before increasing in line with stress during the strain-hardening, softening, and residual strength stages. Initial permeability increased with an increased bedding angle. Permeability was also found to be parabolically related to radial strain.

(4) The compression strength of the samples initially decreased and then rose with an increased bedding angle. Compression strength was largest at a bedding angle of 0° , followed by the compression strength when the bedding angle was 90° . Under these circumstances, splitting failure occurred in the samples. When the bedding angle was 60° , the compression strength of the samples was smallest, resulting in sliding failure along the bedding plane. The sample with a bedding angle of 30° exhibited compound splitting and shear failure.

Author Contributions: Y.C. designed and performed the tests and wrote the paper; X.L. and B.L. analyzed the data.

Funding: This work is supported by the China Postdoctoral Science Foundation under grant nos. 2017M620048 and 2018T110103.

Conflicts of Interest: The authors declare no conflict of interest.

References

1. Yang, D.; Qi, X.; Chen, W.; Wang, S.; Dai, F. Numerical investigation on the coupled gas-solid behavior of coal using an improved anisotropic permeability model. *J. Nat. Gas Sci. Eng.* **2016**, *34*, 226–235. [[CrossRef](#)]
2. Liu, R.; Li, B.; Jiang, Y. Critical hydraulic gradient for nonlinear flow through rock fracture networks: the roles of aperture, surface roughness, and number of intersections. *Adv. Water Resour.* **2016**, *88*, 53–65. [[CrossRef](#)]
3. Liu, R.; Li, B.; Jiang, Y. A fractal model based on a new governing equation of fluid flow in fractures for characterizing hydraulic properties of rock fracture networks. *Comput. Geotech.* **2016**, *75*, 57–68. [[CrossRef](#)]
4. Liu, R.; Jiang, Y.; Li, B.; Wang, X. A fractal model for characterizing fluid flow in fractured rock masses based on randomly distributed rock fracture networks. *Comput. Geotech.* **2015**, *65*, 45–55. [[CrossRef](#)]
5. Rodrigues, C.F.; Laiginhas, C.; Fernandes, M.; Sousa, M.J.L.D.; Dinis, M.A.P. The Coal Cleat System: A new approach to its study. *J. Rock Mech. Geotech. Eng.* **2014**, *6*, 208–218. [[CrossRef](#)]
6. Alexis, D.A.; Karpyn, Z.T.; Ertekin, T.; Crandall, D. Fracture permeability and relative permeability of coal and their dependence on stress conditions. *J. Unconv. Oil Gas Resour.* **2015**, *10*, 1–10. [[CrossRef](#)]
7. An, H.; Wei, X.R.; Wang, G.X.; Massarotto, P.; Wang, F.Y.; Rudolph, V.; Golding, S.D. Modeling anisotropic permeability of coal and its effects on CO₂ sequestration and enhanced coalbed methane recovery. *Int. J. Coal Geol.* **2015**, *152 Pt B*, 15–24. [[CrossRef](#)]
8. Beamish, B.B.; Crosdale, P.J. Instantaneous outbursts in underground coal mines: An overview and association with coal type. *Int. J. Coal Geol.* **1998**, *35*, 27–55. [[CrossRef](#)]
9. Chen, Y.; Wei, K.; Liu, W.; Hu, S.; Hu, R.; Zhou, C. Experimental characterization and micromechanical modelling of anisotropic slates. *Rock Mech. Rock Eng.* **2016**, *49*, 3541–3557. [[CrossRef](#)]
10. Dewhurst, D.N.; Siggins, A.F. Impact of fabric, microcracks and stress field on shale anisotropy. *Geophys. J. Int.* **2006**, *165*, 135–148. [[CrossRef](#)]
11. Korsnes, R.I.; Wersland, E.; Austad, T.; Madland, M.V. Anisotropy in chalk studied by rock mechanics. *J. Petrol. Sci. Eng.* **2008**, *62*, 28–35. [[CrossRef](#)]
12. Li, Y.; Tang, D.; Xu, H.; Meng, Y.; Li, J. Experimental research on coal permeability: The roles of effective stress and gas slippage. *J. Nat. Gas Sci. Eng.* **2014**, *21*, 481–488. [[CrossRef](#)]
13. Liu, J.; Chen, Z.; Elsworth, D.; Miao, X.; Mao, X. Linking gassorption induced changes in coal permeability to directional strains through a modulus reduction ratio. *Int. J. Coal Geol.* **2010**, *83*, 21–30. [[CrossRef](#)]
14. Liu, Q.; Liu, K.; Zhu, J.; Lu, X. Study of mechanical properties of raw coal under high stress with triaxial compression. *Chin. J. Rock Mech. Eng.* **2014**, *33*, 24–34.
15. Louis, L.; David, C.; Metz, V.; Robion, P.; Menendez, B.; Kissel, C. Microstructural control on the anisotropy of elastic and transport properties in undeformed sandstones. *Int. J. Rock. Mech. Min. Sci.* **2005**, *42*, 911–923. [[CrossRef](#)]
16. Ma, Y.; Pan, Z.; Zhong, N.; Connell, L.D.; Down, D.I.; Lin, W.; Zhang, Y. Experimental study of anisotropic gas permeability and its relationship with fracture structure of Longmaxi Shales, Sichuan Basin, China. *Fuel* **2016**, *180*, 106–115. [[CrossRef](#)]
17. Meng, Z.; Li, G. Experimental research on the permeability of high-rank coal under a varying stress and its influencing factors. *Eng. Geol.* **2013**, *162*, 108–117. [[CrossRef](#)]
18. Meng, Y.; Li, Z.; Lai, F. Experimental study on porosity and permeability of anthracite coal under different stresses. *J. Petrol. Sci. Eng.* **2015**, *133*, 810–817. [[CrossRef](#)]
19. Wang, S.; Elsworth, D.; Liu, J. Permeability evolution in fractured coal: The roles of fracture geometry and water-content. *Int. J. Coal Geol.* **2011**, *87*, 13–25. [[CrossRef](#)]
20. Wang, K.; Zang, J.; Wang, G.; Zhou, A. Anisotropic permeability evolution of coal with effective stress variation and gas sorption: Model development and analysis. *Int. J. Coal Geol.* **2014**, *130*, 53–65. [[CrossRef](#)]
21. Talesnick, M.L.; Hatzor, Y.H.; Tsesarsky, M. The elastic deformability and strength of a high porosity, anisotropic chalk. *Int. J. Rock Mech. Min. Sci.* **2001**, *38*, 543–555. [[CrossRef](#)]
22. Xu, X.; Sarmadivaleh, M.; Li, C.; Xie, B.; Iglaier, S. Experimental study on physical structure properties and anisotropic cleat permeability estimation on coal cores from China. *J. Nat. Gas Sci. Eng.* **2016**, *35*, 131–143. [[CrossRef](#)]
23. Liu, S.; Wang, Y.; Harpalani, S. Anisotropy characteristics of coal shrinkage/swelling and its impact on coal permeability evolution with CO₂ injection. *Greenh. Gases* **2016**, *6*, 615–632. [[CrossRef](#)]

24. Risnes, R.; Madland, M.V.; Hole, M.; Kwabiah, N.K. Water weakening of chalk—Mechanical effects of water–glycol mixtures. *J. Petrol. Sci. Eng.* **2005**, *48*, 21–36. [[CrossRef](#)]
25. Wang, S.; Elsworth, D.; Liu, J. Permeability evolution during progressive deformation of intact coal and implications for instability in underground coal seams. *Int. J. Rock Mech. Min. Sci.* **2013**, *58*, 34–45. [[CrossRef](#)]
26. Sirdesai, N.N.; Singh, T.N.; Gamage, R. Thermal alterations in the poro-mechanical characteristic of an Indian sandstone—A comparative study. *Eng. Geol.* **2017**, *226*, 208–220. [[CrossRef](#)]



© 2018 by the authors. Licensee MDPI, Basel, Switzerland. This article is an open access article distributed under the terms and conditions of the Creative Commons Attribution (CC BY) license (<http://creativecommons.org/licenses/by/4.0/>).